Influence of carrier lifetimes on the dynamical behavior of quantum-dot lasers subject to optical feedback

Björn Globisch, Christian Otto, Eckehard Schöll, and Kathy Lüdge
Institut für Theoretische Physik, Technische Universität Berlin, Hardenbergstr. 36, 10623 Berlin, Germany
(Received 22 March 2012; published 3 October 2012)

We examine changes in the dynamics of a semiconductor quantum-dot (QD) laser subject to optical feedback that correlate to changes in the QD laser band structure. By employing a microscopic model for the carrier-carrier scattering processes between the QDs and the carrier reservoir we are able to tune the carrier lifetimes in the QDs, e.g., by modifying the QD confinement energies or the pump current. By using numerical continuation methods as well as asymptotic theory we demonstrate that the feedback sensitivity crucially depends on these lifetimes through the damping of the turn-on oscillations, and small lifetimes on the order of this relaxation time scale lead to an increased feedback resistivity. Thus intelligent band structure engineering can lead to stable continuous wave operation of the laser over a large parameter range.

DOI: 10.1103/PhysRevE.86.046201 PACS number(s): 05.45.−a, 85.35.Be, 42.55.−f

I. INTRODUCTION

Self assembled quantum-dot (QD) lasers are promising candidates for future applications in optical communications devices [1]. Compared to their quantum well (QW) counterparts, they exhibit a lower and less temperature-dependent threshold current, a smaller line width enhancement factor α, and less sensitivity to optical feedback. The last property is especially important in fiber optical telecom applications. Therefore, a lot of experimental and theoretical work has been done to identify the parameters that have the strongest impact on the stability properties of a laser subject to optical feedback [2–4].

In this paper we consider a five-variable rate equation model that combines in a semiclassical approach a Lang-Kobayashi-type field equation [5] with microscopically calculated scattering rates in the carrier rate equations [2,3]. In contrast to simpler models [6,7] we separately treat electrons and holes. Within our model it is possible to derive an analytical condition for the critical feedback strength below which the laser is guaranteed to be stable [4]. According to this relation the parameters that mainly determine the stability properties of the laser are the line width enhancement factor α as well as frequency ω^{RO} and damping Γ^{RO} of the relaxation oscillations. The latter critically depends upon the energy band structure of the QD device and upon the pump current resulting in different scattering-induced lifetimes of the carriers in the QD [8,9]. Hence, it is the purpose of this paper to investigate the destabilizing bifurcations of the QD laser subject to optical feedback focusing on different scattering-induced carrier lifetimes in the QD. They can be implemented directly in our model by a variation of the energy band structure relative to the embedding quantum well carrier reservoir or by varying the pump current. We will show that it is even possible to keep the laser in its continuous wave (CW) regime for the full range of the considered feedback strength by a careful adjustment of these parameters. The investigation is motivated by our work on optically injected QD lasers [10], where we found a strong dependence of the frequency-locking behavior on the QD size and composition and thus on the band structure.

Our paper is organized as follows: Before we perform any numerical bifurcation studies we introduce the laser model and the nonlinear scattering rates in Sec. II. In Sec. III we motivate the numerical bifurcation studies presented in Sec. IV by some important relations derived in analytical investigations of the saddle-node and Hopf bifurcations of the basic solutions of the laser equations. Here we show that position and shape of Hopf bifurcation lines critically depend on the scattering-induced carrier lifetimes, while the appearance of saddle-node bifurcations is not affected by these parameters. Hence, we aim to shift the Hopf bifurcation lines in parameter space such that there exists always at least one basic solution of the laser equations over the full range of the considered bifurcation parameters. The result is a laser that never leaves the desired CW regime. In Sec. V we will verify the analytic results of Sec. III by direct comparison with numerically calculated bifurcation lines before we summarize our results in Sec. VI.

II. LASER MODEL

In this paper we consider the dimensionless electron-hole rate equation model with external optical feedback previously introduced in Refs. [2,3]. The schematic picture of the setup is shown in Fig. 1. In the QD laser model, the carriers are first injected into the two-dimensional carrier reservoir (QW) before being captured by the QDs. A schematic plot of the considered band structure is shown in Fig. 2. The nonlinear rate equations describe the dynamics of the complex electrical field amplitude $\mathcal{E}$ in the slowly varying envelope approximation, the charge carrier densities per unit area in the QD, n_e and n_h, and the carrier densities per unit area in the QW, w_e and w_h (e and h stand for electrons and holes, respectively). Electrical field amplitude $\mathcal{E}$, photon number N_{ph}, QD carrier densities $\rho_{e/h}$, and QW carrier densities $W_{e/h}$ are defined by

$$\mathcal{E} = \sqrt{N_{\mathrm{ph}}}e^{i\phi}, \quad \rho_{e,h} = n_{e,h}/(2N_a^{QD}), \tag{1}$$

$$N_{\mathrm{ph}} = An_{\mathrm{ph}}, \quad W_{e/h} = w_{e,h}/(2N^{QD}). \tag{2}$$

Here N_a^{QD} denotes the density per unit area of the active QDs and N^{QD} the total QD density, as given by experimental surface imaging. The factor 2 accounts for spin degeneracy. As a result of the size distribution and material composition fluctuations of the QDs, the gain spectrum is inhomogeneously broadened,

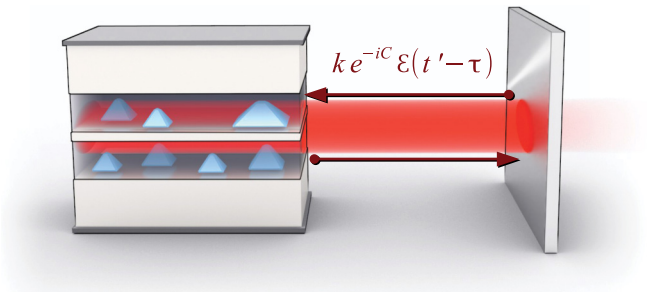

FIG. 1. (Color online) Scheme of a QD laser subject to optical feedback. Light is coupled back into the internal laser cavity after a single round trip in the external cavity.

and only a subgroup (density N_a^{QD}) of all QDs (density N^{QD}) matches the mode energies for lasing. The photon density per unit area is denoted by n_{ph}, and A is the in-plane area of the QW. The full system of delay differential equations reads

$$\mathcal{E}' = \tfrac{1}{2}(1+i\alpha)[g(\rho_e+\rho_h-1)-1]\mathcal{E}(t') + k e^{-iC}\mathcal{E}(t'-\tau), \tag{3}$$

$$\rho_e' = \gamma\big[-\rho_e\tau_e^{-1} + s_e^{\mathrm{in}} - w(\rho_e+\rho_h-1)N_{\mathrm{ph}} - \rho_e\rho_h\big], \tag{4}$$

$$\rho_h' = \gamma\big[-\rho_h\tau_h^{-1} + s_h^{\mathrm{in}} - w(\rho_e+\rho_h-1)N_{\mathrm{ph}} - \rho_e\rho_h\big], \tag{5}$$

$$W_e' = \gamma\big[J+\rho_e\tau_e^{-1} - s_e^{\mathrm{in}} - cW_eW_h\big], \tag{6}$$

$$W_h' = \gamma\big[J+\rho_h\tau_h^{-1} - s_h^{\mathrm{in}} - cW_eW_h\big]. \tag{7}$$

In these equations time $t' = t/\tau_{ph}$ is measured in units of the photon lifetime τ_{ph}, and the prime denotes differentiation with respect to the dimensionless time t'. The nonlinear Coulomb scattering rates $S_e^{\mathrm{in/out}}$ and $S_h^{\mathrm{in/out}}$ are schematically depicted in Fig. 2 and implemented as dimensionless quantities $s_e^{\mathrm{in/out}} = S_e^{\mathrm{in/out}}/W$ and $s_h^{\mathrm{in/out}} = S_h^{\mathrm{in/out}}/W$. Here W is the

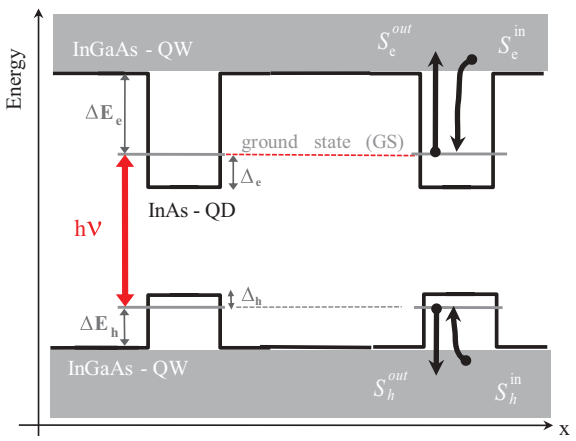

FIG. 2. (Color online) Schematic energy band diagram of QW and QD. ΔE_e and ΔE_h denote the energy spacings of the QW band edge and the QD ground state (GS) for electrons and holes. $h\nu$ marks the GS lasing energy, and Δ_e, Δ_h label the distance of the QD GS from the bottom of the QD.

Einstein coefficient of spontaneous emission, resulting from incoherent interaction of the QDs with all resonator modes. As these scattering rates describe the microscopic Coulomb scattering processes between carriers of the two-dimensional QW and the QDs they are nonlinear functions of the carrier densities in the QW, W_e and W_h. They are systematically derived in Refs. [9,11]. Since they are calculated numerically for different fixed values of the electron and hole densities in the QW, we use nonlinear fitting functions to obtain continuous functions $s_{e/h}(W_e,W_h)$. These fitting parameters are presented in Appendix B. In Ref. [9] it was shown that the in- and out-scattering rates are not independent but connected by detailed balance relations. Hence, it is sufficient to calculate the in-scattering rates in the framework of a microscopic theory and determine the out-scattering rates through Eqs. (B3) and (B4) given in Appendix B.

Due to the described in- and out-scattering processes between QD and QW we obtain nonconstant carrier lifetimes $\tau_{e/h} = (s_{e/h}^{\mathrm{in}} + s_{e/h}^{\mathrm{in}})^{-1}$, which are also nonlinear functions of the carrier densities W_e and W_h in the QW. The order of magnitude of τ_e and τ_h will be an important parameter to understand the different dynamical behavior of the laser in certain scenarios. The small parameter $\gamma = W/(2\kappa) = \mathcal{O}(10^{-3})$ appears in all carrier rate equations and denotes the ratio of the photon lifetime $\tau_{\mathrm{ph}} = (2\kappa)^{-1}$ to the radiative carrier lifetime W^{-1}. Note that the time W^{-1} results from radiative losses due to spontaneous emission processes and must not be confused with the carrier lifetimes $\tau_{e/h}$ resulting from carrier-carrier scattering processes. Due to the smallness of γ the turn-on dynamics of the QD laser show damped relaxation oscillations that are typical for class B lasers (see Fig. 3) [12].

In Eq. (3)–(7) spontaneous emission processes in the QDs are approximated by bimolecular recombination, i.e., $\rho_e\rho_h$. Analogously, the spontaneous recombination rate in the QW is described by cW_eW_h with the normalized band-band recombination coefficient $c = 2B^S N^{\mathrm{QD}}/W$. B_S denotes the band-band recombination coefficient in the QW. The induced processes of absorption and emission are modeled by a linear gain $g(\rho_e+\rho_h-1)$ with the linear gain coefficient $g = 2Z_a^{\mathrm{QD}}\bar{W}/(2\kappa)$ and the carrier inversion $(\rho_e+\rho_h-1)$ in the QD. Here $Z_a^{\mathrm{QD}} = a_L A N_a^{\mathrm{QD}}$ denotes the number of active QDs inside the waveguide, a_L is the number of self-organized QD layers, and $w = \bar{W}/W$ is the ratio of the Einstein coefficient of induced and spontaneous emission, i.e., coherent and incoherent interaction of the QDs with the resonator modes. In previous publications [3,4,8,9,13] a different value for $\bar{W}$ was implemented. This leads to a rescaling of the photon number $N_{\mathrm{ph}} = |\mathcal{E}|^2$ by the factor $w = \bar{W}/W$ in all subsequent equations of this paper. One has to consider this rescaling if the results of this paper are compared to those of previous publications. The derivation of $\bar{W}$ is given in Appendix A.

Carriers are injected into the QW by an electrical current, which is modeled by the dimensionless pump current density $J = j/(2e_0N^{\mathrm{QD}}W)$, where e_0 denotes the elementary charge. The line width enhancement factor α in Eq. (3) models the phase-amplitude coupling of the electric field $\mathcal{E}$. For QD lasers this quantity α is problematic because it cannot account for the independent dynamics of resonant (ρ_e,ρ_h) and nonresonant (w_e,w_h) charge carriers [14,15] and eventually neglects a degree of freedom of the dynamics. It was, however, shown

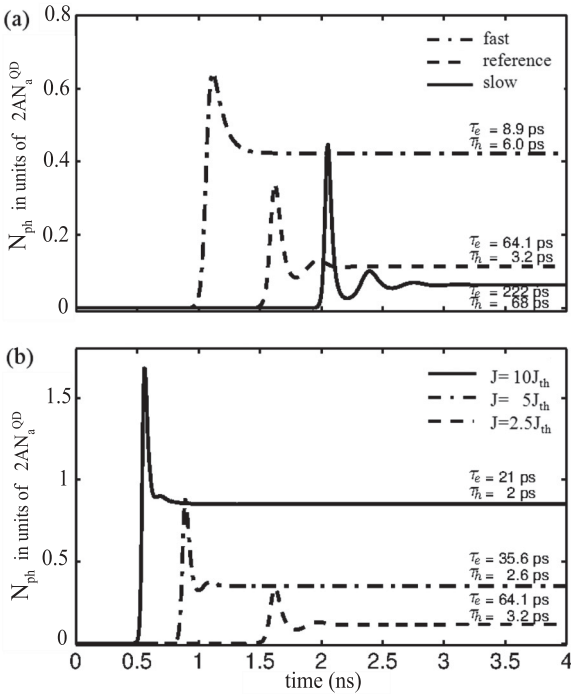

FIG. 3. Turn-on dynamics of the QD laser without optical feedback. (a) The pump current is kept constant at $J = 2.5J_{\text{th}}$, and the QD-QW band structures are changed in agreement with Table I. Using fast, reference, and slow scattering rates leads to the dot-dashed, dashed, and solid turn-on curves. (b) The reference QD-QW band structure is fixed, and the pump current varies from $J = 2.5J_{\text{th}}$ (dashed) via $J = 5J_{\text{th}}$ (dot-dashed) to $J = 10J_{\text{th}}$ (solid) The steady state scattering-induced electron and hole lifetimes $\tau_{e/h}$ label each curve. Parameters are as in Table II.

that QD laser models based on an α parameter still lead reliable results as long as only the transitions between stable and unstable behavior, i.e., Hopf and saddle-node bifurcations, are investigated [15]. Since this is the focus of our paper we choose α to be constant but keep in mind that it may vary with the operation conditions. The optical feedback is expressed by the last term in Eq. (3). This corresponds to the established Lang-Kobayashi model of external optical feedback first published in Ref. [5]. The light is coupled back into the device with the dimensionless feedback strength $k = K/(2\kappa\tau_{\text{in}})$ and the feedback phase $C \equiv \omega_{\text{th}}\tau$. Since K is a dimensionless feedback parameter that varies from zero to one, we will use K instead of k in our subsequent investigations. τ_{in} and τ denote the internal and external cavity round-trip time, respectively, and ω_{th} is the frequency of the solitary laser at lasing threshold in units of t'.

Figure 1 shows a schematic picture of the QD laser structure and the external cavity modeled by a simple mirror. Although being completely determined by ω_{th} and τ the feedback phase C is treated as an independent parameter since small variations of the external cavity length cause a variation of the phase C over its full range $[0, 2\pi]$ while the external round-trip time τ is hardly affected by these fluctuations. This is a well-established procedure in the analysis of semiconductor lasers subject to optical feedback [3,16–18]. Hence, we always consider C as a free parameter in our two-parameter bifurcation diagrams presented in Secs. IV and V.

TABLE I. Confinement energies for three different QD-QW band structures and the associated steady state carrier lifetimes at $J = 2.5J_{\text{th}}$ as investigated throughout this paper. The corresponding turn-on dynamics is depicted in Fig. 3.

Name	ΔE_e [meV]	ΔE_h [meV]	τ_e [ps]	τ_h [ps]
Slow	140	120	222.0	68.0
Reference	210	50	64.1	3.2
Fast	74	40	8.9	6.0

The purpose of this paper is to discuss the impact of different carrier lifetimes on the laser dynamics under optical feedback. These different carrier lifetimes can be introduced into the simulations by using different nonlinear scattering rates $s_{e/h}^{\text{in/out}}$. In our microscopic model these rates are not simply a parameter but are calculated within a detailed picture of the QW-QD band structure (Fig. 2). Since the magnitude of the nonlinear in- and out-scattering rates strongly depends on the QD-QW band structure, changing the confinement energies $\Delta E_{e/h}$ results in very different scattering rates and carrier lifetimes. The three QD structures considered in this paper are characterized by the confinement energies and resulting carrier lifetimes listed in Table I.

The corresponding turn-on dynamics of the QD laser without optical feedback ($k = 0$) obtained by numerical integration of Eqs. (3)–(7) is shown in Fig. 3(a). The assumed values of all numerical parameters appearing in Eqs. (3)–(7) are listed in Table II. If not stated otherwise they will be used for all subsequent simulations and path continuations.

The important difference between the three turn-on curves in Fig. 3(a) is the damping of the relaxation oscillations. The dashed-dotted line that corresponds to small energy spacings $\Delta E_e = 74$ meV, $\Delta E_h = 40$ meV between QW and QD for both carrier types shows an exponential decay of the photon density to its steady state value. This is the characteristical turn-on behavior of a class A laser corresponding to similar lifetimes of carriers and photons ($\tau_e = 8.9$ ps, $\tau_h = 6.0$ ps, $\tau_{\text{ph}} = 10.0$ ps). Hence, this QD structure is labeled *fast* because short carrier lifetimes imply fast carrier exchange between QD and QW. Note that the radiative carrier lifetimes W^{-1} is equal for all QD structures considered here. For the QD structure named *slow* (solid line) we observe damped relaxation oscillations that are indicative of a class

TABLE II. Parameters appearing in Eqs. (3)–(7). Physical parameters that correspond to dimensionless parameters are given in Table III of Appendix A.

Symbol	Value	Meaning
g	3.96	Linear gain parameter
γ	7×10^{-3}	Ratio of photon to carrier lifetime
w	1.5×10^{-4}	Ratio of Einstein coefficients of induced and spontaneous emission
k	$K/2.4$	Rescaled feedback strength
τ	16	External cavity round-trip time
c	1.54	Spontaneous and nonradiative losses
J/J_{th}	2.50	Ratio of current to current at laser threshold

B laser. In this case we assume relatively large confinement energies $\Delta E_e = 140$ meV and $\Delta E_h = 120$ meV resulting in long carrier scattering lifetimes compared to the photons ($\tau_e = 222$ ps, $\tau_h = 68$ ps, $\tau_{\rm ph} = 10$ ps). The turn-on dynamic of the *reference* QD structure shows relaxation oscillations that are more strongly damped than in the case of slow carriers but still observable. In this case there is a time-scale separation between the underlying electron and hole scattering lifetimes ($\tau_e = 64$ ps, $\tau_h = 3$ ps, $\tau_{\rm ph} = 10$ ps). It is called *reference* as it resembles the behavior found in common QD laser experiments [13]. It was also investigated in previous dynamical studies of the QD laser with optical feedback [2,3].

The impact of the pump current J on the turn-on dynamics is investigated within Fig. 3(b), where for clarity only the reference scattering rates are considered. Note that the dashed line in panel (a) corresponds to the dashed line in panel (b). By increasing the pump current from $2.5J_{\rm th}$ to $10J_{\rm th}$ the damping of the relaxation oscillations increases while the corresponding steady state scattering-induced carrier lifetimes $\tau_{e/h}$ decrease. Thus we can conclude from Fig. 3 that higher pump currents as well as smaller energy spacings between QW and QD in the band structure lead to smaller carrier lifetimes $\tau_{e/h}$ and thus to larger damping of the turn-on oscillations.

Before we start our numerical bifurcation analysis of the QD laser with optical feedback in Sec. IV we will summarize some important analytical results in the next section. The scattering-induced carrier lifetimes $\tau_{e/h}$ discussed in this section will play an important role in the following analytical and numerical investigations.

III. ANALYTICAL RESULTS

In this section we briefly summarize the results of a geometric bifurcation analysis of Eqs. (3)–(7) performed in Ref. [3] based on the results of Refs. [19,20]. The basic solutions of Eqs. (3)–(7) with nontrivial photon number $N_{\rm ph} = |\mathcal{E}|^2 \neq 0$ are called external cavity modes (ECMs). They correspond to constant photon and carrier densities and a phase of the electric field amplitude that varies linearly in time (continuous-wave light output of the laser). The existence of this type of solution is caused by the S^1-symmetry of Eqs. (3)–(7) that has been investigated in detail in Ref. [21] for a QW laser with optical feedback. The transformation

$$\mathcal{E} \to c\mathcal{E} \text{ with } \{c \in \mathbb{C} : \|c\| = 1\}, \tag{8}$$

i.e., a rotation of $\mathcal{E}$ in the complex plane, leaves Eqs. (3)–(7) invariant. Thus, solutions of Eqs. (3)–(7) must show this rotational invariance in the complex plane too. Therefore, the basic solutions of the dynamical equation (3) are rotating waves. By separating Eq. (3) in amplitude $N_{\rm ph}$ and phase ϕ of the complex field amplitude $\mathcal{E}$ via $\mathcal{E}(t) = \sqrt{N_{\rm ph}(t)}e^{i\phi(t)}$ we obtain the following two equations:

$$N'_{\rm ph} = \{g[\rho_e + \rho_h + 1] - 1\}N_{\rm ph} + 2k\sqrt{N_{\rm ph}(t'-\tau)N_{\rm ph}}\cos(\Delta\phi + C), \tag{9}$$

$$\phi' = \frac{\alpha}{2}\{g[\rho_e + \rho_h + 1] - 1\} - k\sqrt{\frac{N_{\rm ph}(t'-\tau)}{N_{\rm ph}}}\sin(\Delta\phi + C), \tag{10}$$

with $\Delta\phi = \phi(t') - \phi(t'-\tau)$. In terms of N_{ph} and ϕ an ECM solution is of the form

$$(N_{\rm ph}, \phi) = (N_{{\rm ph},s}, \Delta\omega_s t'). \tag{11}$$

Here $\Delta\omega_s$ denotes the time-constant ECM frequency deviation from the threshold frequency $\omega_{\rm th}$ of the laser. Together with Eqs. (9) and (10) the following two expressions can be derived

$$-2k\cos(\Delta\omega_s\tau + C) = \{g[\rho_e + \rho_e + 1] - 1\}, \tag{12}$$

$$\Delta\omega_s + k\sin(\Delta\omega_s\tau + C) = \frac{\alpha}{2}\{g[\rho_e + \rho_e + 1] - 1\}. \tag{13}$$

Inserting Eq. (12) into Eq. (13) yields

$$\Delta\omega_s = -k[\alpha\cos(\Delta\omega_s\tau + C) + \sin(\Delta\omega_s\tau + C)]. \tag{14}$$

In Eq. (12) one can observe the well known gain-clamping in semiconductor lasers [22]; i.e., the sum of the electron and hole density in the QDs is constant above threshold. With the help of some trigonometric identities and the definition of an effective feedback strength $K_e \equiv k\tau\sqrt{1+\alpha^2}$ Eq. (14) can be rewritten as

$$\Delta\omega_s\tau = -K_e\sin[\Delta\omega_s\tau + C + \arctan(\alpha)]. \tag{15}$$

The number of solutions of this transcendental equation for $\Delta\omega_s$ determines the number of existing ECMs. The right-hand side of Eq. (15) is a sinusoidal oscillation with frequency $\Delta\omega_s$ while the left-hand side is a linear function of $\Delta\omega_s$. Thus, the solutions of Eq. (15) are the intersection points of a straight line and a periodic function. From this geometrical point of view its obvious that new solutions of Eq. (15) are created in pairs if the slope of both sides coincides [19]. This condition reads

$$-\frac{1}{K_e} = \cos[\Delta\omega_s\tau + C + \arctan(\alpha)]. \tag{16}$$

We note that for $K_e < 1$ Eq. (16) has no solution, and for $K_e > 1$ at least two or even more ECMs may exist. Since K_e directly depends on α and K, the number of existing ECMs increases with these parameters. Thus, we will consider the influence of α and K on the laser dynamics in our subsequent bifurcation analysis. The pairwise appearance of new solutions is indicative of a *saddle-node bifurcation*. Therefore, Eq. (16) can be treated as the determining equation for saddle-node bifurcation points [19]. If we reorganize Eq. (16) we get an analytic expression for the saddle-node bifurcation line in the (C,K) plane

$$C_n^{\rm SN}(k) = \pm\left[\sqrt{K_e^2 - 1} + \arccos\left(-\frac{1}{K_e}\right)\right] - \arctan(\alpha) + 2n\pi, \tag{17}$$

with $n \in \mathbb{Z}$. This equation neither depends on the scattering rates $s_{e/h}^{\rm in/out}$ nor on the pump current J. Thus, the position of a saddle-node bifurcation point in the (C,K) plane is neither influenced by the energetic structure of the QD device nor by the pump current. Note that Eq. (17) is even equivalent to that given in Ref. [19] for the QW laser because no quantity specific of QDs appears. Our next step is to show analytically that the position of Hopf bifurcation points depends explicitly on the scattering rates $s_{e/h}^{\rm in/out}$. This motivates the detailed numerical investigation presented in Sec. IV, where we determine the

relative positions of Hopf and saddle-node bifurcation lines in the (C,K) plane depending on the QD confinement energies and the pump current. The basic idea of the asymptotic analysis of Eqs. (3)–(7) is to exploit the smallness of the parameter $\gamma = \mathcal{O}(10^{-3})$ [23]. The extensive asymptotic expansions have been performed in Ref. [4] for the reference and the slow scattering rates (see Fig. 3). (The analysis of the impact of the scattering-induced carrier lifetimes $\tau_{e/h}$ is possible by treating $s_{e/h}^{\text{in/out}}$ as constant parameters. The value of these steady state scattering constants determines the order of magnitude of the terms containing them and hence influences the appearance of these terms in the hierarchy of the asymptotic expansion.) For the subsequent discussions it is sufficient to present the results. In both cases (reference and slow scattering rates) the critical feedback strength k^H at which the ECM solution is destabilized in a Hopf bifurcation is given by

$$k^H = \frac{-2\Gamma^{\text{RO}}}{\sqrt{1+\alpha^2}[1-\cos(\omega^{\text{RO}}\tau)]\cos[C+\Delta\omega_s\tau-\arctan(\alpha)]} \tag{18}$$

with the frequency of the relaxation oscillations ω^{RO} and their damping rate Γ^{RO}. The latter two quantities are given by

$$\omega_{\text{slow}}^{\text{RO}} = \sqrt{2wN_{\text{ph}}^*\gamma}, \tag{19}$$

$$\Gamma_{\text{slow}}^{\text{RO}} = \Gamma^{\text{QW}} + \frac{\gamma}{4}\left[\frac{1}{\tau_e}+\frac{1}{\tau_h}\right], \tag{20}$$

$$\omega_{\text{ref}}^{\text{RO}} = \sqrt{wN_{\text{ph}}^*\gamma}, \tag{21}$$

$$\Gamma_{\text{ref}}^{\text{RO}} = \frac{\gamma}{2}\left[\tau_e^{-1}+wN_{\text{ph}}^*+\rho_h^*+\frac{wN_{\text{ph}}^*}{\gamma}\tau_h\right]. \tag{22}$$

In these expressions the asterisk superscript labels steady state values of the solitary laser, and $\Gamma^{\text{QW}} = \gamma/2[1+g^{-1}+2wN_{\text{ph}}^*]$ is the damping rate of the relaxation oscillations for the QW laser. In Ref. [20] the authors derived an equation for the Hopf bifurcation of a QW laser with optical feedback in the framework of an asymptotic analysis. That equation exhibits the same functional dependencies as Eq. (18). Primarily, one can derive two general properties from Eq. (18). The stability of the QD laser increases on the one hand with higher damping of the relaxation oscillations Γ^{RO} and on the other hand with smaller α factors.

We recall that the α parameter in QD lasers is sensitive both to the position of the emission wavelength with respect to the gain maximum and to the pump current, while in the considered regime it does not depend on the internal scattering processes [15]. Thus it can be varied within an experiment. For the two sets of scattering rates considered in our asymptotic analysis the frequency of the relaxation oscillations ω^{RO} depends only on the steady state photon density N_{ph}^* and scales with $\sqrt{\gamma}$. However, the damping rate of the relaxation oscillations Γ^{RO} is a function of the scattering-induced carrier lifetimes τ_e and τ_h. This indicates that the appearance of Hopf bifurcation points strongly depends on the scattering-induced carrier lifetimes through the damping of the turn-on oscillations. As we already mentioned in the discussion of Fig. 3 the two main factors that influence the scattering-induced carrier lifetimes are the QD confinement energies and the pump current. Hence, we expect different behavior of the QD laser subject to optical feedback depending on QD structure and operation condition. As an example a smaller gain, e.g., due to less layers of QDs, would lead to higher steady state values of the carrier densities, which in turn decrease the carrier lifetimes and thus increase the turn-on damping as indicated in Eqs. (20) and (22). Consequently a smaller gain increases the feedback tolerance. Further, the analytic results summarized in the equation for the critical feedback strength [Eq. (18)] could also be useful to determine an approximate α factor from feedback experiments if the damping of the turn-on oscillations is exactly known.

Since the argument of the cosine in the denominator of Eq. (18) contains the ECM frequency shift $\Delta\omega_s$ and $\Delta\omega_s = \Delta\omega_s(k)$ [see Eq. (15)], Eq. (18) depends implicitly upon k. However, with the help of some trigonometric identities and Eq. (15) it is possible to reorganize Eq. (18) such that the Hopf bifurcation line in the (C,K) plane can be calculated analytically by the following relation (for details of the derivation see Appendix C):

$$C_n^H(k) = \arctan(\alpha) \pm \arccos\left(\frac{-\mathcal{G}}{K_e^H}\right) - \frac{2\alpha\mathcal{G}}{1+\alpha^2} \pm \frac{1-\alpha^2}{1+\alpha^2}\sqrt{\left(K_e^H\right)^2-\mathcal{G}^2} + 2n\pi, \tag{23}$$

with $\mathcal{G} = 2\Gamma^{\text{RO}}\tau/[1-\cos(\omega^{\text{RO}}\tau)]$, the effective feedback strength $K_e^H = k^H\tau\sqrt{1+\alpha^2}$ at a Hopf bifurcation point and $n \in \mathbb{Z}$. The above rearrangement of Eq. (18) gives us the opportunity to compare our numerically obtained two-parameter bifurcation diagrams directly with the results of the asymptotic analysis. This will be done in detail in Sec. V.

IV. NUMERICAL BIFURCATION ANALYSIS

In order to use numerical continuation methods for calculating bifurcation diagrams of Eqs. (3)–(7) one has to resolve the S^1 symmetry [16]. As mentioned in the last section, an ECM solution is not unique due to the invariance of the solution under transformations of the type of Eq. (8). It is well known from Refs. [16,18] that the substitution

$$\mathcal{E} \to A(t')e^{ibt} \tag{24}$$

with the additional parameter $b \in \mathbb{R}$ and $A(t') = x(t') + iy(t')$ leads to two dynamic equations for $x(t')$ and $y(t')$

$$\begin{aligned} x'(t') = {} & \frac{1}{2}\{g[\rho_e(t')+\rho_h(t')-1]-1\}x(t') + by(t') \\ & - \frac{\alpha}{2}\{g[\rho_e(t')+\rho_h(t')-1]-1\}y(t') \\ & + k\cos(C+b\tau)x(t'-\tau) \\ & + k\sin(C+b\tau)y(t'-\tau), \\ y'(t') = {} & \frac{1}{2}\{g[\rho_e(t')+\rho_h(t')-1]-1\}y(t') - bx(t') \\ & + \frac{\alpha}{2}\{g[\rho_e(t')+\rho_h(t')-1]-1\}x(t') \\ & - k\sin(C+b\tau)x(t'-\tau) \\ & + k\cos(C+b\tau)y(t'-\tau). \end{aligned} \tag{25}$$

Since the phase of the electric field amplitude is still not uniquely defined in these equations the free parameter b is used to set $y(t') = y(t' - \tau) \equiv y_s = 0$. Now, one can calculate an ECM solution as a fixed point of Eqs. (25) together with Eqs. (4)–(7) and the additional condition $y_s = 0$.

The subsequent numerical bifurcation diagrams are calculated with the continuation packages DDE-BIFTOOL [24] and KNUT [25].

A. One-parameter bifurcation set

To start our numerical bifurcation analysis we first compare the results of direct numerical integration of Eqs. (3)–(7) and the path continuation in DDE-BIFTOOL as the feedback strength K is varied. We contrast a relatively large α factor ($\alpha = 3$) with $\alpha = 0.9$ in order to point out the advantages of a small α that QD lasers are supposed to have [26]. The remaining important bifurcation parameters are set to $C = \pi$, $\tau = 16$, and $J = 2.5 J_{\text{th}}$. These values correspond to a short external cavity of 2.4 cm and a pump current density clearly above threshold J_{th}. Figure 4 shows the one-parameter bifurcation diagrams of the photon number N_{ph} (normalized to $2AN_a^{\text{QD}}$) versus the bifurcation parameter K for $\alpha = 0.9$ in panels (a) and (c) and $\alpha = 3$ in panels (b) and (d). In the upper panel (direct numerical integration) local extrema of the photon density are plotted for each K after transients have died out. The differences between gray and black points in Fig. 4(a) and 4(b) result from different choices of the initial conditions in the numerical simulations. The results depicted in gray correspond to solutions where those values of the photon and carrier densities that were used as an initial condition on the delay interval that have been calculated as final results of the lower feedback strength in the previous simulation (up-sweep of K). Experimentally this could be realized by increasing the reflectivity of a mirror while the pump current is not switched off. In the same sense, the black points represent the decrease of the feedback strength from $K = 1$ to $K = 0$ (down-sweep of K). By distinguishing these two ways of feedback implementation it is possible to identify hysteresis effects.

The lower panel of Fig. 4 shows the bifurcations of the steady state solutions calculated with path continuation methods. For clarity we plot only the maxima of the photon number $N_{\text{ph}}^{\max}$ (normalized to $2AN_a^{\text{QD}}$). Solid and dashed lines denote stable and unstable steady state solutions (ECMs), respectively. Vertical dashed lines facilitate the comparison of Hopf (circles) and saddle-node bifurcation points (squares) in panels (b) and (d) with the bifurcation diagrams in panels (a) and (c). Exemplarily we continue the periodic solution that emerges from the Hopf bifurcation of the first ECM for $\alpha = 0.9$ and $\alpha = 3$. Period-doubling and Torus bifurcations of these periodic solutions are marked with triangles and stars, respectively.

First, we note that there exist fewer ECM solutions for $\alpha = 0.9$ compared to $\alpha = 3$ if K is increased. This is predicted directly by Eq. (14). Second, one observes for all of the

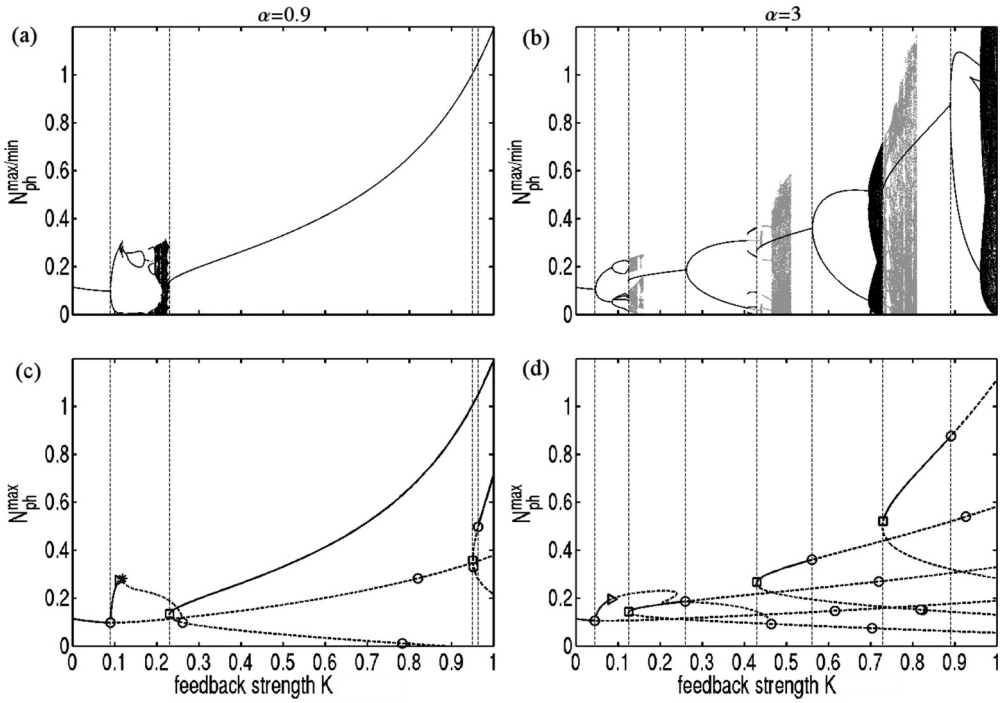

FIG. 4. One-parameter bifurcation diagrams of the photon number N_{ph} (normalized to $2AN_a^{\text{QD}}$) vs feedback strength K for direct numerical integration [(a), (b)] and path continuation with DDE-BIFTOOL and KNUT [(c), (d)]. In the upper panels maxima and minima of the photon density $N_{\text{ph}}^{\min/\max}$ (normalized to $2AN_a^{\text{QD}}$) are plotted, in the lower panels only maxima $N_{\text{ph}}^{\max}$ are shown. The α factor is set to $\alpha = 0.9$ (left column) and to $\alpha = 3$ (right column). In (a) and (b) gray points indicate results for an upsweep of K, and black points result from down-sweep of K. In (c) and (d) Hopf, saddle-node, torus, and period doubling bifurcation points are denoted by dots, squares, stars, and triangles, respectively. Stable solutions are printed as solid lines, unstable solutions as dashed lines. Vertical dashed lines facilitate comparison. Further parameter are fixed at $C = \pi$, $\tau = 16$, and $J = 2.5 J_{\text{th}}$. Shown are the results for the reference scattering rates (see Fig. 3 and Table I).

bifurcation diagrams that the solitary solution is initially stable for small values of K before it is destabilized in a Hopf bifurcation (circle). The emerging periodic solution can be clearly identified in the diagrams obtained by direct integration [Fig. 4(a) and 4(b)] as well as in the results of path continuation in panels (c) and (d). For a detailed analysis of the bifurcations of periodic solutions and the chaotic regimes see Ref. [3]. Our extension of the analysis presented there is the continuation of the first periodic solution after it has been destabilized in a torus or periodic-doubling bifurcation. In Fig. 4(c) and 4(d) one observes that the periodic solution created in the Hopf bifurcation of the first ECM solution vanishes in a Hopf bifurcation of the unstable branch (antimode) of the subsequent ECM. These bifurcation bridges between two consecutive ECM solutions have been studied extensively in Ref. [16] for the QW laser. In that paper the authors suspected that the existence of bifurcation bridges is generic as new modes and antimodes appear. This assumption is supported by our results.

From now on we will focus on the steady state bifurcations. In Fig. 4(c) and 4(d) it can be seen that the next pair of ECM solutions is created in a saddle-node bifurcation with one stable and one unstable ECM. The stable upper branch is again destabilized in a Hopf bifurcation. In general, we note that all the upper branches emerging from a saddle-node bifurcation point are initially stable and are destabilized for higher feedback strength K in a Hopf bifurcation. The clear difference of upsweep (gray) and downsweep (black) of K in Fig. 4(a) and 4(b) can be explained directly with the use of the results of the path continuation. For increasing K each upper ECM branch becomes unstable in a Hopf bifurcation, and the emerging periodic orbit bifurcates via period doubling. When the next pair of ECM solutions is created in the saddle-node bifurcation the periodic solution that emerges from the previous ECM solution does not reach the attractor of the new ECM directly, but needs a further increase of K to do so. Instead, for decreasing K the ECM vanishes in a saddle-node bifurcation, and the laser directly jumps to the only stable solution that exists, i.e., the periodic orbit. The consequence of this bistability of a periodic orbit and an ECM solution is that the existence of a stable ECM solution does not necessarily mean that the laser will operate in the CW regime in an experimental setup. This strongly depends on the experimental implementation of the feedback.

B. Two-parameter bifurcations

We now investigate the bifurcations of the ECMs in the (C,K) plane for the three different QD device structures introduced in Sec. II. The upper panel of Fig. 5 shows two-parameter bifurcation diagrams for $\alpha = 0.9$ calculated for the implementation of fast (a), reference (b), and slow (c) scattering rates. The lower panel is organized identically with $\alpha = 3$. Hopf and saddle-node bifurcation lines are depicted as solid and dashed lines, respectively. The bifurcation curves are drawn dark when supercritical, and light when subcritical. The number of stable ECM solutions is expressed by the shaded areas. White shading means no stable ECM solution, light gray areas correspond to one stable ECM and dark gray labels regions of bistability of two ECM solutions. The one-parameter bifurcation diagrams we discussed before in Fig. 4 correspond to a vertical line for $C = \pi$ in Fig. 5(b) and 5(e). If we begin our analysis with the upper panel of Fig. 5 we note that the solitary solution is stable for all $C \in (-\pi,\pi)$ below a certain feedback strength K. (Note the 2π periodicity of all bifurcation lines.) The destabilization of the solitary ECM occurs in a Hopf bifurcation for all the three QD energy structures. The important difference between Fig. 5(a), 5(b), and 5(c) is the position of the destabilizing Hopf bifurcation line with respect to the saddle-node bifurcation line. As we stated in Sec. III the saddle-node bifurcation lines are not affected by changing the QD energy structure. Hence, they exhibit the same shape in all the three plots. However, the shape of the Hopf bifurcation lines is drastically different for the three QD structures. In Fig. 5(a) the Hopf line always appears above the saddle-node line. Therefore, we can find at least one stable ECM solution for all $K \in (0,1)$ and $C \in (-\pi,\pi)$. Thus, the laser never leaves the region of time-constant photon density emission. Figure 5(b) shows a quite different situation for the case of implemented reference rates. One may find two white shaded areas that indicate the absence of any stable ECM solution. For $C \in (\pi/2,\pi)$ and $K < 0.3$ the bistability region of Fig. 5(a) disappears because the Hopf bifurcation line is moved to smaller values of K. The same occurs for the Hopf line at $C \in (-\pi,\pi/2)$ and $K \in (0.1,0.7)$. Here the laser is destabilized in a Hopf bifurcation before a new stable ECM solution exists, resulting in oscillatory and chaotic behavior of the photon density. The highest K for which the solitary ECM solution of the laser is still stable in the full range of C is $K < 0.1 \equiv K_c$. Tuning the QD size to even slower rates leads to the bifurcation diagram shown in Fig. 5(c). The unstable, white regions are even larger than in panel (b), and the $K_c \approx 0.06$ indicates higher sensitivity to optical feedback for this QD structure. In the lower panel of Fig. 5 ($\alpha = 3$) the same general conclusions derived by analyzing the upper panel can be drawn. The fast QD structure exhibits the highest critical feedback strength K_c and the most extended regions of bistability. Both, K_c and the bistability regions decrease for the reference and slow QD structures. Due to the increased number of possible ECM solutions for the higher α factor it is no longer possible to guarantee the existence of one stable ECM solution for the full range of C and K in Fig. 5(d) as it was possible for $\alpha = 0.9$. However, one is able to minimize the unstable regions for the fast QD structure compared to reference and slow. Here one has to keep in mind from the study of Fig. 4 that the existence of a stable ECM solution does not mean automatically that the laser performs a CW operation. If there exists a stable periodic solution that was created in a Hopf bifurcation of the last ECM in addition to the now stable ECM it crucially depends on the initial conditions in a numerical simulation, or the implementation of the feedback in an experiment, which solution is favored by the laser. In order to determine those areas in the (C,K) plane where the laser is guaranteed to be stable, one has to find the bifurcation point that connects the periodic solution with the next ECM solution. This is a quite challenging task and not considered in this paper. Hence, it is important to stress here that the light-gray shaded areas label areas in the (C,K) plane where it is possible to prepare the laser in the CW regime.

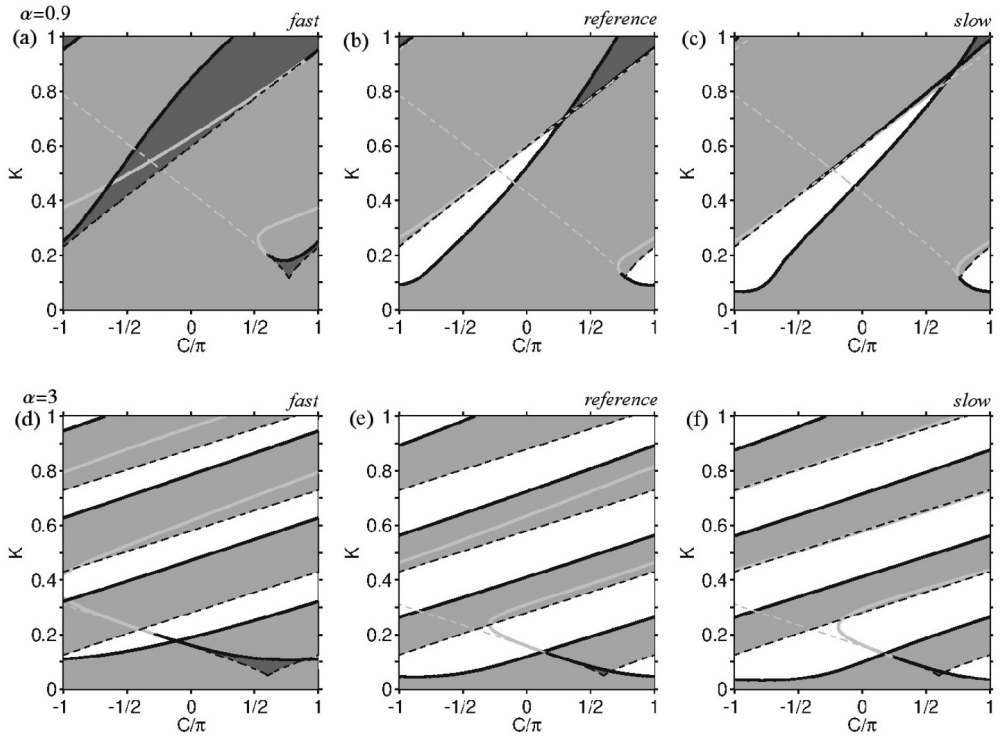

FIG. 5. Two-parameter bifurcation diagrams of the ECM solutions in the plane of the feedback phase C vs feedback strength K. (a)–(c) $\alpha = 0.9$, (d)–(f) $\alpha = 3$. Panels (a) and (d) correspond to the set of fast scattering rates, (b) and (e) to reference rates, and (c) and (f) to the slow rates (see also Table I). Hopf bifurcation lines are drawn as solid lines, saddle-node bifurcation lines as dashed lines. Bifurcation lines are displayed dark when supercritical and light when subcritical. Shading marks the number of stable ECM solutions. White indicates no stable ECM, light gray marks one stable ECM solution and dark gray denotes bistability of two ECM solutions. The pump current is fixed at $2.5J_{\text{th}}$.

In the previous discussion we observed that the confinement energy distribution of the QD laser has a large impact on its sensitivity to optical feedback. As we mentioned in Sec. III the determining equation for the saddle-node bifurcation lines [Eq. (17)] neither depends on the scattering rates nor on the pump current. So far, we have fixed the pump current at $2.5J_{\text{th}}$ and analyzed the influence of the scattering rates on the ECM bifurcations. Our next step is to change the pump current to a different, fixed value and compare the bifurcation scenarios with Fig. 5. Note that our microscopic modeling of the carrier density-dependent scattering rates allows us to change the pump current without adjusting any time scale parameter. Figure 6 shows the bifurcation diagrams for $\alpha = 0.9$ with implemented fast, reference, and slow scattering rates at a pump current of $J = 5J_{\text{th}}$ (upper panel) and $J = 10J_{\text{th}}$ (lower panel). Here we restrict our numerical analysis to a small α factor since its value for QD lasers is expected to be relatively small [26]. However, it is noted that the general pump current-dependent changes that are discussed in the following can be observed for $\alpha = 3$ as well.

If one compares the upper panel of Fig. 6 with the upper panel of Fig. 5 one can conclude as a first result that the saddle-node bifurcation lines have the same shape for all scattering rates and pump currents as was predicted in Sec. III. The Hopf bifurcation lines instead are shifted towards higher feedback strength K resulting in more extended regions of stability and bistability. Going to even higher currents as shown in the lower panel of Fig. 6 it is striking to see that all white regions disappear as the Hopf lines shift above the saddle-node lines for all QD structures. An explanation can again be given by discussing the nonlinear scattering rates. From Fig. 3(b) we know that an increasing pump current leads to a reduction of the scattering-induced lifetimes $\tau_{e/h}$ and increases the steady state photon density N^*_{ph}. If we reconsider the results of the asymptotic analysis presented in Sec. III we can explain the reduced sensitivity of the laser subject to optical feedback directly by the dependencies of Eq. (22):

$$\Gamma^{\text{RO}}_{\text{ref}} = \frac{\gamma}{2}\left[\tau_e^{-1} + wN^*_{\text{ph}} + \rho^*_h + \frac{wN^*_{\text{ph}}}{\gamma}\tau_h\right]. \tag{26}$$

One observes that the damping of the relaxation oscillations increases with the steady state photon and hole density, N^*_{ph} and ρ^*_h, respectively. Logically, these two quantities will increase for higher pump currents. Equation (26) also implies that $\Gamma^{\text{RO}}_{\text{ref}}$ will increase for decreasing electron lifetime τ_e but for increasing hole lifetimes τ_h. From Fig. 3(a) one obtains that both the steady state values of τ_e and τ_h decrease for increasing J. However, the relative decrease of τ_e from $J = 2.5J_{\text{th}}$ to $J = 10J_{\text{th}}$ is by a factor of 2 higher than the decrease of τ_h. Therefore, with the help of our analytic results we can explain the lower sensitivity of the laser towards optical feedback with increasing pump currents by a reduction of the scattering-induced carrier lifetimes τ_e and τ_h.

From Fig. 5 and Fig. 6 we conclude that it is possible to increase the stability of the QD laser towards optical feedback by adjusting both the pump current and the QD-QW band structure of the device.

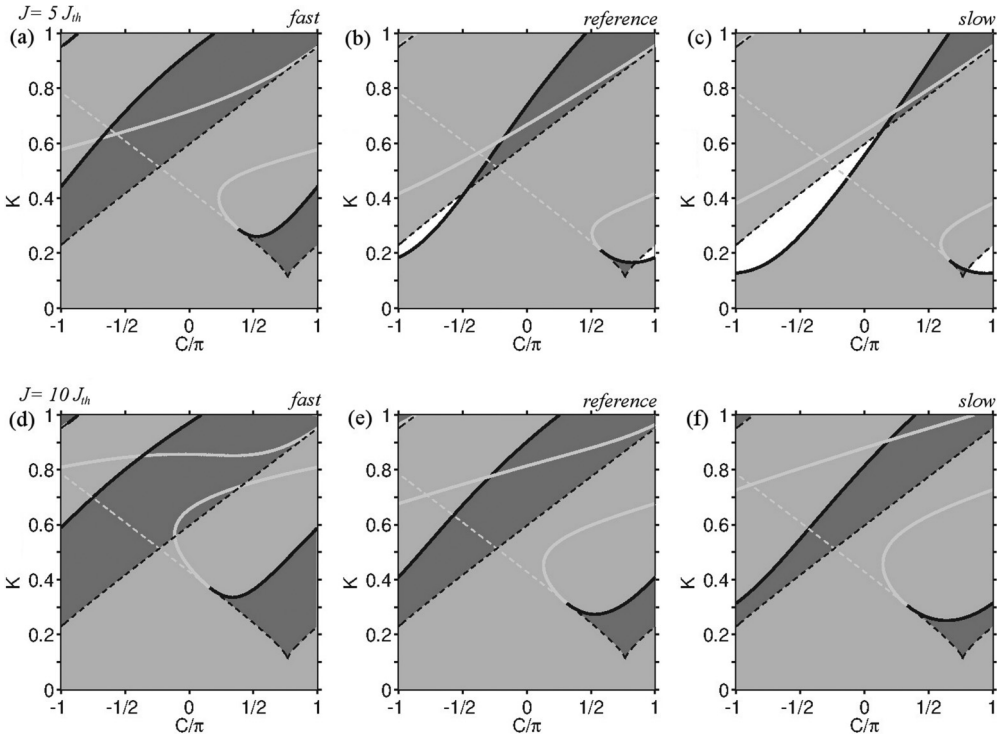

FIG. 6. Same as Fig. 5 for (a)–(c): $J = 5J_{\text{th}}$ and (d)–(f): $J = 10J_{\text{th}}$. The α factor is fixed at $\alpha = 0.9$.

A last interesting remark concerns the shape of the first Hopf bifurcation line in all two-parameter bifurcation diagrams we investigate here. One observes that these lines (light and dark solid lines in Figs. 5 and 6) appear as a loop in the lower right part of the two-parameter bifurcation diagrams. (The size of this loop drastically increases with the pump current. Compare Fig. 6 upper and lower panels.) For $C = \pi$ and low feedback two distinct Hopf bifurcation points are found in all two-parameter bifurcation diagrams. That is a supercritical Hopf point for lower feedback strength and a subcritical Hopf point for higher feedback strength. A detailed investigation of the subcritical Hopf point reveals that it coincides with that Hopf bifurcation on the antimode of the subsequent ECM we mentioned in the previous subsection. That means that the bifurcation bridge that emerges from the supercritical Hopf point disappears in that subcritical Hopf point we see in all two parameter bifurcation diagrams for $C = \pi$. If the feedback phase C is now decreased from $C = \pi$ the supercritical and subcritical Hopf bifurcation points collide with each other. This behavior is another indication of the connection between two subsequent ECM solutions through bifurcation bridges [see Fig. 4(c) and 4(d)] that are created in a supercritical Hopf bifurcation and vanish in a subcritical Hopf bifurcation.

V. COMPARISON OF NUMERICAL AND ASYMPTOTIC RESULTS

In this section we compare the numerically calculated first Hopf bifurcation line in the (C, K) plane with the analytic prediction for two different carrier lifetime scenarios. The analytical formula [Eqs. (23)] was presented in Sec. III and is derived in Ref. [4]. One of the most important approximations applied in the derivation processes is the assumption of small optical feedback, i.e., $k = \mathcal{O}(\gamma)$. This corresponds to an interval $K \in [0,0.02]$ where the Hopf bifurcation occurs in order to ensure good agreement between numerical and analytical results. From Figs. 5 and 6 it can be seen that the minimal critical feedback strength of the first Hopf bifurcation is close to $K^H = 0.1$ for $\alpha = 0.9$. Thus, the condition of $k = \mathcal{O}(\gamma)$ is never fulfilled for small line width enhancement factors $\alpha = 0.9$. In contrast, for $\alpha = 3$ the critical feedback strength is in the vicinity of the required interval. Hence, we will consider the relatively large line width enhancement factor $\alpha = 3$ in this section.

Figure 7(a) shows the numerically obtained Hopf bifurcation line from Fig. 5(e) as a solid curve and the computed Hopf line obtained from Eq. (23) as a dashed curve. For clarity we plot the bifurcation lines in the truncated interval $K \in [0,0.25]$ and omit the shading. In the small feedback regime we find good agreement between the two bifurcation lines. The shape as well as the position of the analytically obtained bifurcation line compares well with the numerical solution for C in the vicinity of $\pm\pi$. The agreement of the two curves becomes worse for C close to zero because the critical feedback strength moves to higher values of K. However, even in this regime the analytical solution reproduces the shape of the numerical solution and can be used as a worst-case estimate. In Fig. 7(b) the results for the slow scattering rates are shown. The conclusions drawn from Fig. 7(a) also apply here. The asymptotic analysis of the laser equations in the regime of relatively large scattering induced carrier lifetimes τ_e and τ_h (slow scattering rates) predicts the appearance of the destabilizing Hopf bifurcation in accordance with the numerical analysis. Hence, we can

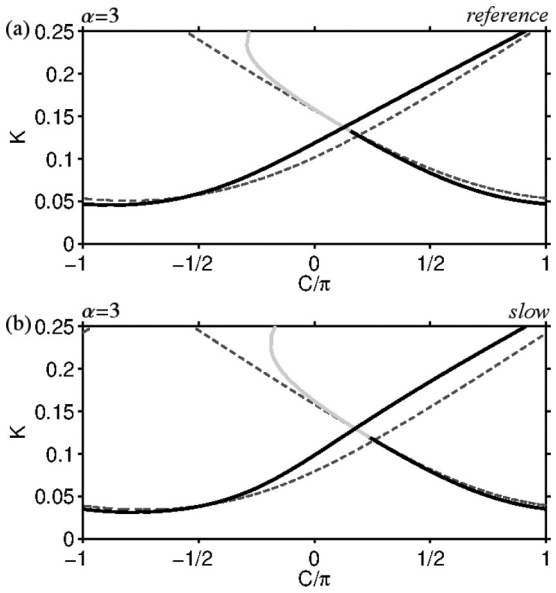

FIG. 7. Comparison between numerical (solid) and analytical (dashed) results for the Hopf bifurcation line in the (C,K) plane. $J = 2.5J_{\text{th}}$ and $\alpha = 3$: (a) reference, (b) slow scattering rates.

conclude that the parameters that appear in Eq. (23) mainly contribute to the stability properties of the laser subject to optical feedback and may be used to optimize the stability properties. Especially the line width enhancement factor α as well as the scattering-induced carrier lifetimes $\tau_{e/h}$ have to be controlled in order to obtain a device with the desired properties.

Our dynamical analysis also shows that the knowledge of the laser turn-on dynamics is sufficient to predict the stability boundaries (here the first Hopf bifurcation) of the QD laser even if complicated carrier dynamics is involved. This result is robust under parameter variation and useful for experimental characterization since turn-on experiments are much easier to perform than feedback experiments. Of course, changes in the gain parameter or in the scattering lifetimes have a large impact on the turn-on dynamics as explicitly discussed in Eqs. (20) and (22), but, after all, a simplified modeling approach that uses a reduced number of dynamic variables for the solitary QD laser will also lead to reliable results for the stability boundaries of the feedback problem as long as the correct turn-on dynamics of the laser is reproduced. Instead, the detailed shape of the bifurcation diagram (as seen in Fig. 4) that goes beyond the stability information given in Figs. 5 and 6 depends on the details of the carrier dynamics and will change if, e.g., excited states are included or if the amplitude-phase coupling is implemented beyond the description with a constant α factor.

VI. CONCLUSION

In this paper we have demonstrated that the stability properties of a QD laser are influenced crucially by the scattering-induced carrier lifetimes. In our QD laser model we assume nonlinear Coulomb scattering rates that enable us to compute the carrier lifetimes numerically based on a microscopic model. Hence, we obtain carrier lifetimes that change with the pump current and the considered QD-QW band structure. Therefore, we can investigate changes of these parameters without using the carrier lifetimes as fit parameters. Within this model we have identified both analytically and numerically the most important parameters that determine the sensitivity of the QD laser to optical feedback. We propose that the stability towards back reflection of light can be significantly increased on the one hand by a small α factor that might be achieved by adjusting the resonator wavelength, and on the other hand by strongly damped relaxation oscillations that occur, e.g., if the laser is operated at higher pump currents. Further, also optimizing the QD structures and its material compositions leads to better feedback resistivity if a higher damping of the relaxation oscillations is obtained.

ACKNOWLEDGMENTS

We thank B. Lingnau for fruitful discussions. The work of B. Globisch, K. Lüdge, and E. Schöll was supported by DFG in the framework of Sfb 787. C. Otto acknowledges the research training group GRK 1558 for support.

APPENDIX A: DERIVATION OF PHOTO RATE EQUATION

The coherent interaction between a two-level system (e.g., QD) and a light mode can be described by semiconductor Bloch equations. [11,27,28] Eliminating the fast microscopic polarization p of one QD (the probability amplitude for an optical transition) by assuming $\dot{p} = 0$ leads to a quasistatic relation between p and the slowly varying complex amplitude E of the electric field. By further assuming equal energy for light mode and level spacing this relation reads

$$p = -i\frac{\mu E T_2}{\hbar}(\rho_e + \rho_h - 1). \tag{A1}$$

Here μ is the associated dipole moment of the optical transition and T_2 is the lifetime of the microscopic polarization defining the homogeneous line width $\hbar/T_2$ of the levels. The term $(\rho_e + \rho_h - 1)$ describes the inversion of the two-level system with the electron and hole occupation probabilities in the QDs, ρ_e and ρ_h. For the derivation of the photon rate equation we start with the reduced field equation for the electric field [29] without damping,

$$\dot{E} = \frac{i\omega_L \Gamma}{2\varepsilon_0 \varepsilon_{bg}} P, \tag{A2}$$

where ε_0 is the vacuum permittivity, ε_{bg} is the background dielectric constant, and ω_L is the transition frequency of the two-level system. Please see Table III for the numerical values used for the physical parameters. Using the total macroscopic polarization inside one QW layer given by $P = \frac{1}{h^{\text{QW}}} 2N_a^{\text{QD}} \mu p$, and the optical confinement factor Γ perpendicular to the direction of light propagation $\Gamma = \frac{a_L h^{\text{QW}}}{h^w}$ (height h^w of the waveguide, height h^{QW} of the QW layers that contain the self-organized QDs, and number of QW layers a_L), we arrive at the following field equation:

$$\begin{aligned}\dot{E} &= \frac{|\mu|^2 \omega_L T_2 a_L 2N_a^{\text{QD}}}{2\varepsilon_0 \varepsilon_{bg} \hbar h^w}(\rho_e + \rho_h - 1)E \\ &= Z_a^{\text{QD}} \bar{W}(\rho_e + \rho_h - 1)E\end{aligned} \tag{A3}$$

TABLE III. Numerical parameters used in simulations.

Symbol	Value	Meaning
A	4×10^{-5} cm^2	QW in-plane area
N^{QD}	10×10^{10} cm^{-2}	Total QD density
N_a^{QD}	0.3×10^{10} cm^{-2}	Density of active QDs
a_L	15	Number of QD layer
τ_{ec}	160 ps	External cavity round-trip time
τ_{in}	24 ps	Internal cavity round-trip time
B^S	540 ns^{-1} nm^2	QW band-band recombination coefficient
2κ	0.1 ps^{-1}	Optical intensity loss
W	0.7 ns^{-1}	Einstein coefficient of spontaneous emission
$\bar{W}$	0.11 μs^{-1}	Einstein coefficient of induced emission
T	300 K	Carrier temperature

with the Einstein coefficient of induced emission

$$\bar{W} = \frac{|\mu|^2 \omega_L T_2}{\varepsilon_0 \varepsilon_{bg} \hbar V^w}, \tag{A4}$$

which measures the strength of the coherent interaction. $\bar{W}$ depends on the volume of the optical waveguide $V^w = A \cdot h^w$ and on the width of the optical transition $\hbar/T_2$. The number $Z_a^{\mathrm{QD}} = a_L A N_a^{\mathrm{QD}}$ is the number of active QDs inside the waveguide. Rewriting Eq. (A3) for the photon density per unit area $n_{\mathrm{ph}} = |E|^2 \frac{h^w \varepsilon_0 \varepsilon_{bg}}{2\hbar\omega}$ gives

$$\dot{n}_{\mathrm{ph}} = 2 Z_a^{\mathrm{QD}} \bar{W} (\rho_e + \rho_h - 1) n_{\mathrm{ph}}. \tag{A5}$$

In previous publications [2,8,9,13] a different value for $\bar{W}$ was implemented because the QD volume V^{act} was used instead of the optical waveguide volume V^w in Eq. (A4). As a result the geometric optical confinement factor $\Gamma_g = \frac{V^{\mathrm{act}}}{V^w}$ appeared in the equation for the photon density per unit area Eq. (A5), which was somewhat misleading. Because the differing $\bar{W}$ was also used in the carrier equations, those simulations yield a rescaled photon density. Thus, the values for n_{ph} given in Refs. [2,8,9,13] need to be multiplied by 6.6×10^3 to yield the real photon density in the cavity.

The Einstein coefficient for the spontaneous emission can be derived by calculating the incoherent interaction of the two-level system with all resonator modes in the framework of second quantization [29]. It gives $W = \frac{|\mu|^2 \sqrt{\varepsilon_{bg}}}{3\pi \varepsilon_0 \hbar} (\frac{\omega_L}{c})^3$.

APPENDIX B: SCATTERING RATES

The results of the microscopic calculations of the carrier-carrier scattering rates have been fitted with the following functions to enable their use with path continuation software:

$$s_e^{\mathrm{in}}(W_e, W_h) = [\tanh(a_e W_e + b_e)] \sum_{i=1}^{4} \left(c_{e,i} W_e^i + d_{e,i} W_h^i \right), \tag{B1}$$

$$s_h^{\mathrm{in}}(W_e, W_h) = [\tanh(a_h W_e + b_h)] \sum_{i=1}^{4} \left(c_{h,i} W_e^i + d_{h,i} W_h^i \right). \tag{B2}$$

TABLE IV. Fit parameters for the reference rates from Table I.

Coefficient	Value	Coefficient	Value
a_e	-1.836×10^{-5}	a_h	3.326×10^{-5}
b_e	-7.89×10^{-6}	b_h	-8.064×10^{-4}
$c_{e,1}$	-298187.0	$c_{h,1}$	-6886.56
$c_{e,2}$	38 443.3	$c_{h,2}$	-7191.73
$c_{e,3}$	-3287.08	$c_{h,3}$	1117.15
$c_{e,4}$	112.303	$c_{h,4}$	-43.6502
$d_{e,1}$	53 262.5	$d_{h,1}$	-17291.4
$d_{e,2}$	571.696	$d_{h,2}$	-13288.4
$d_{e,3}$	-72.5439	$d_{h,3}$	1000.69
$d_{e,4}$	0.683815	$d_{h,4}$	-52.8802

The parameter values of the coefficients are given in Table IV for the reference rates, in Table V for the fast rates, and in Table VI for the slow rates. Due to the principle of detailed balance, the out-scattering rates can be calculated from the in-scattering rates with the help of a detailed balance relation derived in Ref. [9]:

$$s_e^{\mathrm{out}}(W_e, W_h) = s_e^{\mathrm{in}}(W_e, W_h) e^{\frac{-\Delta E_e}{k_B T}} \left(e^{\frac{2 W_e N^{\mathrm{QD}}}{D_e k_B T}} - 1 \right)^{-1}, \tag{B3}$$

$$s_h^{\mathrm{out}}(W_e, W_h) = s_h^{\mathrm{in}}(W_e, W_h) e^{\frac{-\Delta E_h}{k_B T}} \left(e^{\frac{2 W_h N^{\mathrm{QD}}}{D_h k_B T}} - 1 \right)^{-1}. \tag{B4}$$

In these equations ΔE_e and ΔE_h denote the energy differences between the QD ground states and the QW band edge for electrons and holes (see also Fig. 2). $D_e = m_e/(\pi\hbar)$ and $D_h = m_h/(\pi\hbar)$ are the two-dimensional density of states in the QW with the effective masses of electrons and holes $m_e = 0.43 m_0$ and $m_h = 0.45 m_0$, respectively. k_B is the Boltzmann constant and T the absolute temperature that is fixed at room temperature ($T = 300$ K) in our simulations. Hence, the confinement energies $\Delta E_{e/h}$ from Table I contribute to both the microscopically calculated in-scattering rates and the out-scattering rates obtained from the detailed balance relations (B3) and (B4).

TABLE V. Parameters for the fast rates from Table I.

Coefficient	Value	Coefficient	Value
a_e	-1.73923×10^{-5}	a_h	1.34424×10^{-5}
b_e	-1.30964×10^{-6}	b_h	-3.35376×10^{-4}
$c_{e,1}$	$-707\,607.0$	$c_{h,1}$	-626.353
$c_{e,2}$	106 490.0	$c_{h,2}$	-3077.88
$c_{e,3}$	-8788.67	$c_{h,3}$	356.116
$c_{e,4}$	287.055	$c_{h,4}$	-17.8843
$d_{e,1}$	51 376.6	$d_{h,1}$	-13087.5
$d_{e,2}$	7347.35	$d_{h,2}$	$-15\,153.0$
$d_{e,3}$	-663.515	$d_{h,3}$	1066.2
$d_{e,4}$	17.169	$d_{h,4}$	-55.0711

APPENDIX C: ANALYTICAL HOPF BIFURCATION LINE

In this section we perform the transformation of Eq. (18) into Eq. (23). We start with Eq. (18) (see Sec. III):

$$k^H = \frac{-2\Gamma^{\mathrm{RO}}}{\sqrt{1+\alpha^2}[1-\cos(\omega^{\mathrm{RO}}\tau)]\cos[C+\Delta\omega_s\tau-\arctan(\alpha)]}. \tag{C1}$$

The first step is to introduce the abbreviations:

$$\mathcal{G} = \frac{2\Gamma^{\mathrm{RO}}\tau}{1-\cos(\omega^{\mathrm{RO}}\tau)}, \qquad K_e^H = k^H\tau\sqrt{1+\alpha^2}. \tag{C2}$$

In this notation Eq. (C1) has the form

$$K_e^H = \frac{-\mathcal{G}}{\cos[C+\Delta\omega_s\tau-\arctan(\alpha)]}, \tag{C3}$$

$$\Leftrightarrow \Delta\omega_s\tau = \arctan(\alpha) - C \pm \arccos\left(-\frac{\mathcal{G}}{K_e^H}\right) + 2n\pi. \tag{C4}$$

If one rewrites the ECM condition of Eq. (15) in the same way one obtains

$$\Delta\omega_s\tau = -K_e^H \sin[C+\Delta\omega_s\tau+\arctan(\alpha)]. \tag{C5}$$

Inserting Eq. (C4) into Eq. (C5) leads to

$$\begin{aligned} C = {} & \arctan(\alpha) \pm \arccos\left(-\frac{\mathcal{G}}{K_e^H}\right) \\ & + K_e^H \sin\left\{2\arctan(\alpha) \pm \arccos\left(-\frac{\mathcal{G}}{K_e^H}\right)\right\} \\ & + 2n\pi. \end{aligned} \tag{C6}$$

In order to simplify Eq. (C6) one uses several trigonometric identities for resolving the sine:

$$\sin(x\pm y) = \sin(x)\cos(y) \pm \sin(y)\cos(x), \tag{C7}$$

$$\cos(x\pm y) = \cos(x)\cos(y) \mp \sin(y)\sin(x), \tag{C8}$$

$$\sin[\arctan(x)] = \frac{x}{\sqrt{1+x^2}}, \tag{C9}$$

$$\cos[\arctan(x)] = \frac{1}{\sqrt{1+x^2}}, \tag{C10}$$

TABLE VI. Parameters for the slow rates from Table I.

Coefficient	Value	Coefficient	Value
a_e	-2.6612×10^{-5}	a_h	1.94259×10^{-5}
b_e	-1.6475×10^{-6}	b_h	-4.74478×10^{-4}
$c_{e,1}$	−363 381	$c_{h,1}$	−3601.34
$c_{e,2}$	50 519.5	$c_{h,2}$	−15193.1
$c_{e,3}$	−4290.71	$c_{h,3}$	1441.14
$c_{e,4}$	146.18	$c_{h,4}$	−47.7236
$d_{e,1}$	69 984.1	$d_{h,1}$	−19 129.2
$d_{e,2}$	−74.2397	$d_{h,2}$	−5584.61
$d_{e,3}$	−86.6277	$d_{h,3}$	435.245
$d_{e,4}$	1.65736	$d_{h,4}$	−27.6885

$$\sin[\arccos(x)] = \sqrt{1-x^2}. \tag{C11}$$

With the help of these identities one can expand the sine in Eq. (C6) as follows:

$$\begin{aligned} & \sin\left\{2\arctan(\alpha) \pm \arccos\left(-\frac{\mathcal{G}}{K_e^H}\right)\right\} \\ & \overset{(C7)}{=} \sin[2\arctan(\alpha)]\cos\left[\arccos\left(-\frac{\mathcal{G}}{K_e^H}\right)\right] \\ & \quad \pm \cos[2\arctan(\alpha)]\sin\left[\arccos\left(-\frac{\mathcal{G}}{K_e^H}\right)\right]. \end{aligned}$$

Using

$$\sin[2\arctan(\alpha)] \overset{(C7)}{=} 2\sin[\arctan(\alpha)]\cos[\arctan(\alpha)] \overset{(C9),(C10)}{=} \frac{2\alpha}{1+\alpha^2}$$

and

$$\cos[2\arctan(\alpha)] \overset{(C8)}{=} \cos^2[\arctan(\alpha)] - \sin^2[\arctan(\alpha)] \overset{(C9),(C10)}{=} \frac{1-\alpha^2}{1+\alpha^2}$$

one obtains

$$\begin{aligned} & \sin\left\{2\arctan(\alpha) \pm \arccos\left(-\frac{\mathcal{G}}{K_e^H}\right)\right\} \\ & = -\frac{2\alpha\mathcal{G}}{K_e^H(1+\alpha^2)} \pm \frac{1-\alpha^2}{1+\alpha^2}\sin\left[\arccos\left(-\frac{\mathcal{G}}{K_e^H}\right)\right] \\ & \overset{(C11)}{=} -\frac{2\alpha\mathcal{G}}{K_e^H(1+\alpha^2)} \pm \frac{1-\alpha^2}{1+\alpha^2}\sqrt{1-\frac{\mathcal{G}^2}{\left(K_e^H\right)^2}} \\ & = \frac{1}{K_e^H}\left\{-\frac{2\alpha\mathcal{G}}{1+\alpha^2} \pm \frac{1-\alpha^2}{1+\alpha^2}\sqrt{\left(K_e^H\right)^2-\mathcal{G}^2}\right\}. \end{aligned}$$

Inserting this result into equation Eq. (C6) leads to

$$\begin{aligned} C_n^H(k) = {} & \arctan(\alpha) \pm \arccos\left(\frac{-\mathcal{G}}{K_e^H}\right) - \frac{2\alpha\mathcal{G}}{1+\alpha^2} \\ & \pm \frac{1-\alpha^2}{1+\alpha^2}\sqrt{\left(K_e^H\right)^2-\mathcal{G}^2} + 2n\pi. \end{aligned} \tag{C12}$$

[1] D. Bimberg, M. Grundmann, and N. N. Ledentsov, *Quantum Dot Heterostructures* (John Wiley & Sons, New York, 1999).

[2] C. Otto, K. Lüdge, and E. Schöll, Phys. Status Solidi B **247**, 829 (2010).

[3] C. Otto, B. Globisch, K. Lüdge, E. Schöll, and T. Erneux, Int. J. Bif. Chaos **22**, 1250246 (2012).

[4] K. Lüdge, in *Nonlinear Laser Dynamics—From Quantum Dots to Cryptography*, edited by K. Lüdge (Wiley-VCH, Weinheim, 2012), p. 3.

[5] R. Lang and K. Kobayashi, IEEE J. Quantum Electron. **16**, 347 (1980).

[6] D. O'Brien, S. P. Hegarty, G. Huyet, and A. V. Uskov, Opt. Lett. **29**, 1072 (2004).

[7] G. Huyet, D. O'Brien, S. P. Hegarty, J. G. McInerney, A. V. Uskov, D. Bimberg, C. Ribbat, V. M. Ustinov, A. E. Zhukov, S. S. Mikhrin, A. R. Kovsh, J. K. White, K. Hinzer, and A. J. SpringThorpe, Phys. Status Solidi B **201**, 345 (2004).

[8] K. Lüdge and E. Schöll, Eur. Phys. J. D **58**, 167 (2010).

[9] K. Lüdge and E. Schöll, IEEE J. Quantum Electron. **45**, 1396 (2009).

[10] J. Pausch, C. Otto, E. Tylaite, N. Majer, E. Schöll, and K. Lüdge, New J. Phys. **14**, 053018 (2012).

[11] N. Majer, K. Lüdge, and E. Schöll, Phys. Rev. B **82**, 235301 (2010).

[12] K. Lüdge, E. Schöll, E. A. Viktorov, and T. Erneux, J. Appl. Phys. **109**, 103112 (2011).

[13] K. Lüdge, R. Aust, G. Fiol, M. Stubenrauch, D. Arsenijević, D. Bimberg, and E. Schöll, IEEE J. Quantum Electron. **46**, 1755 (2010).

[14] S. Melnik, G. Huyet, and A. V. Uskov, Opt. Express **14**, 2950 (2006).

[15] B. Lingnau, K. Lüdge, W. W. Chow, and E. Schöll, Proc. SPIE **8432**, 84321J (2012).

[16] B. Haegeman, K. Engelborghs, D. Roose, D. Pieroux, and T. Erneux, Phys. Rev. E **66**, 046216 (2002).

[17] T. Heil, I. Fischer, W. Elsäßer, B. Krauskopf, K. Green, and A. Gavrielides, Phys. Rev. E **67**, 066214 (2003).

[18] K. Green, Phys. Rev. E **79**, 036210 (2009).

[19] V. Rottschäfer and B. Krauskopf, Int. J. Bif. Chaos **17**, 1575 (2007).

[20] A. M. Levine, G. H. M. van Tartwijk, D. Lenstra, and T. Erneux, Phys. Rev. A **52**, R3436 (1995).

[21] B. Krauskopf, G. H. M. van Tartwijk, and G. R. Gray, Opt. Commun. **177**, 347 (2000).

[22] G. H. M. van Tartwijk and D. Lenstra, Quantum Semiclass. Opt. **7**, 87 (1995).

[23] T. Erneux and P. Glorieux, *Laser Dynamics* (Cambridge University Press, Cambridge, 2010).

[24] K. Engelborghs, T. Luzyanina, and D. Roose, ACM Trans. Math. Softw. **28**, 1 (2002).

[25] R. Szalai, KNUT: A continuation and bifurcation software for delay-differential equations, 2009 (unpublished).

[26] T. C. Newell, D. J. Bossert, A. Stintz, B. Fuchs, K. J. Malloy, and L. F. Lester, IEEE Photonics Technol. Lett. **11**, 1527 (1999).

[27] M. Wegert, N. Majer, K. Lüdge, S. Dommers-Völkel, J. Gomis-Bresco, A. Knorr, U. Woggon, and E. Schöll, Semicond. Sci. Technol. **26**, 014008 (2011).

[28] N. Majer, S. Dommers-Völkel, J. Gomis-Bresco, U. Woggon, K. Lüdge, and E. Schöll, Appl. Phys. Lett. **99**, 131102 (2011).

[29] W. W. Chow and S. W. Koch, *Semiconductor-Laser Fundamentals* (Springer, Berlin, 1999).